IEEE Open Journal of Nanotechnology

Received 13 August 2023; revised 8 November 2023; accepted 8 November 2023. Date of publication 10 November 2023; date of current version 24 November 2023. The review of this paper was arranged by Associate Editor M. Tanemura.

Digital Object Identifier 10.1109/OJNANO.2023.3331974

Observations of Aharonov-Bohm Conductance Oscillations in CVD-Grown Graphene Rings at 4K

ZITAO TANG [1], SIWEI CHEN [1], CYNTHIA I. OSUALA [2], ABDUS SALAM SARKAR [1], GRZEGORZ HADER [3], ARON CUMMINGS [4], STEFAN STRAUF [2,5], CHUNLEI QU [2,5], AND EUI-HYEOK YANG [1,5] (Senior Member, IEEE)

[1]Department of Mechanical Engineering, Stevens Institute of Technology, Hoboken, NJ 07030 USA
[2]Department of Physics, Stevens Institute of Technology, Hoboken, NJ 07030 USA
[3]US Army DEVCOM, Armaments Center, Picatinny Arsenal, NJ 07806 USA
[4]Catalan Institute of Nanoscience and Nanotechnology (ICN2), 08193 Barcelona, Spain
[5]Center for Quantum Science and Engineering, Stevens Institute of Technology, Hoboken, NJ 07030 USA

CORRESPONDING AUTHOR: EUI-HYEOK YANG (e-mail: eyang@stevens.edu).

This work was supported in part by the US Army-DEVCOM under Grants W15QKN18D0040, DOW15QKN21F0272, HQ003419D0003, and DO HQ003421F0515. *(Zitao Tang and Siwei Chen contributed equally to this work.)*
This article has supplementary downloadable material available at https://doi.org/10.1109/OJNANO.2023.3331974, provided by the authors.

ABSTRACT We present the observations of Aharonov-Bohm (AB) oscillations in chemical vapor deposition (CVD)-grown graphene rings via magnetotransport measurements at 4K under out-of-plane external magnetic fields up to +/−2.1 T. Incorporating a baseline subtraction of the original conductance data allowed us to observe two-terminal conductance oscillations with a spacing of ΔB_{AB} of 3.66 to 32.9 mT from the ring with an inner radius of 200 nm and arm-width of 400 nm, and spacing of ΔB_{AB} from 2.1 mT to 8.2 mT from the ring with an inner radius of 400 nm and an arm-width of 400 nm. The fast-Fourier transform (FFT) data showed AB oscillation periods, with the interval of the *h/e* fundamental mode given by 30/T to 273/T for the ring with the inner radius of 200 nm and arm-width of 400 nm, and 122/T to 488/T for the ring with the inner radius of 400 nm. The broad spreading of FFT peaks is due to the aspect ratio of the inner radius r_1 and the width w of the ring, $r/w \sim 1$. Systematic numerical simulations were performed to elucidate the relation between the AB oscillation frequency and the geometry of the ring. This work shows AB oscillations in CVD-grown graphene rings at an elevated temperature (4K).

INDEX TERMS Chemical vapor deposition (CVD)-grown graphene, ring structures, Aharonov-Bohm (AB) oscillations, fast-Fourier transform (FFT).

I. INTRODUCTION

Matter-wave interferometry represents a powerful tool to demonstrate quantum phenomena and their applications in optical imaging and sensing [1], [2], [3], [4]. For example, the Aharonov-Bohm (AB) effect is a fundamental phenomenon of quantum interference related to the transmission of charged particles (e.g., electrons) through a closed loop pierced by magnetic flux [5], [6], [7], [8], [9]. AB oscillation is related to the difference in the phase shifts acquired along the two paths, which is proportional to the magnetic flux of the enclosed area divided by the flux quantum *h/e* where *h* is Planck's constant and *e* is the charge of the electron. Unlike traditional effects that generate interference patterns, such as the Sagnac or Mach-Zehnder effect [8], [10], [11], [12], which require modifying the optical path length of one interferometer arm with respect to the other, the AB effect only requires a static magnetic field that is enclosed by and perpendicular to the electron path.

In recent years, 2D materials have become a focus of intense research due to their unique physical and chemical properties, ascribed to their dimensionality and band structure [13], [14], [15], [16]. While the AB effect has been studied

in various 3D and 2D materials, such as common metals, phosphorene, and p-type GaAs [17], [18], [19], [20], [21], graphene is an ideal material for studying the AB effect owing to its long coherence length of electrons. The electron coherence length in graphene has been measured to be 3–5 μm at 260 mK, and 765 nm-1.25 μm at 4K [22], prompting several studies on the AB effect in graphene rings [23], [24], [25], [26], [27], [28], [29], [30]. Huefner et al. studied the magnetoresistance of a side-gated ring structure etched out of mechanically exfoliated monolayer graphene. It showed changes in the relative phases of the wavefunctions in the interfering paths [23], [29]. Smirnov et al. demonstrated that the period and amplitude of the observed AB oscillations are independent of the sign of the applied gate voltage, which shows the equivalence between unipolar and dipolar interference [24]. Recher et al. conducted a theoretical study of the AB effect and broken valley degeneracy in circular graphene ring structures with smooth edges and hexagonal ring structures with zigzag edges [25]. Schelter et al. reviewed the electronic and transport properties in graphene ring structures [26]. Dauber et al. showed ballistic electron guiding and magnetic focusing in hexagonal boron nitride (hBN)-encapsulated graphene ring structures and AB effects in graphene rings over different magnetic field ranges, including at high magnetic fields near quantum Hall plateaus [27]. Russo et al. studied the temperature dependence of the AB oscillation amplitude of graphene rings and the phase coherent length for different magnetic field ranges [28]. Wurm et al. studied the conductance of mesoscopic graphene rings in a perpendicular magnetic field using numerical calculations based on a tight-binding model [30]. To date, mechanically exfoliated graphene has been used to demonstrate the AB effect in various ring geometries at temperatures ranging from 36 mK to 3.5K.

Here, we show the observations of AB conductance oscillations in chemical vapor deposition (CVD)-grown graphene rings at 4K. The graphene structures were etched in ring shapes and characterized by measuring magnetoconductance oscillations under out–of–plane magnetic fields. We employ a denoising process to extract the AB oscillations and use the fast-Fourier-transform (FFT) to show the correlation between frequency intervals and the ring geometries. We also perform systematic numerical simulations to elucidate the relationship between the AB oscillation frequency and the ring's geometry: the ring's width and the lead's width.

II. EXPERIMENTAL METHODS

A. MATERIALS AND FABRICATION

CVD-grown graphene was acquired from Graphenea, a commercial product of 1 cm × 1 cm monolayer graphene encapsulated between a 100 μm-thick porous organic polymer substrate and a 100 nm-thick acrylate-based polymer layer on the top. To fabricate our device, first, the electrodes were fabricated via an electron beam lithography (EBL) process on a SiO_2/Si substrate, followed by separating graphene from the bottom polymer layer via soaking in water to transfer graphene onto the electrode substrate. The SiO_2/Si substrate

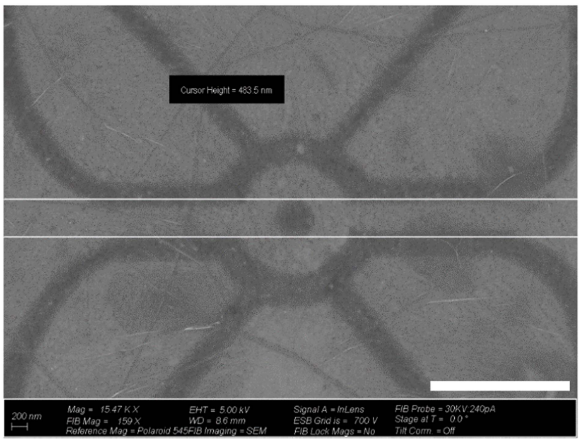

(a)

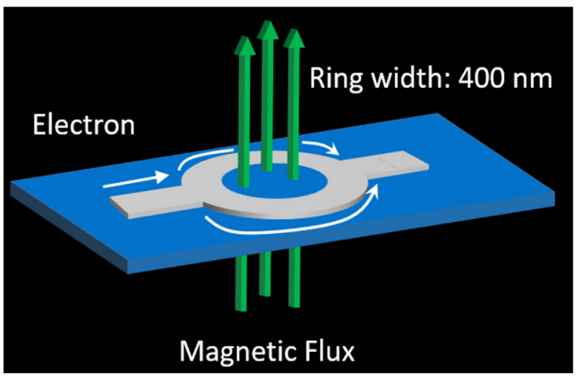

(b)

FIGURE 1. Graphene ring for the Aharonov-Bohm (AB) effect. (a) Scanning electron microscope (SEM) image of a ring-shaped device etched in graphene. The scale bar is 1 μm. (b) Schematic of the electron transport via a graphene ring giving rise to the AB effect.

with graphene atop was soaked in acetone for 12 hours to remove the remaining (top) polymer layer. Then, another electron beam lithography was performed to define graphene rings aligned with electrodes. The Raman spectrum of graphene is shown in Fig. 1S. The G peak appears around 1580 cm^{-1}, which corresponds to the primary in-plane vibrational mode of graphene, and the 2D peak appears at around 2690 cm^{-1}, which corresponds to the second-order overtone of a different in-plane vibration mode of graphene [31]. The peak intensity ratio of 2D peak and G peak (I_{2D}/I_G) ratio of monolayer graphene ranges from 2.1 to 3 [32], [33], [34]; our graphene is around 2.8, showing that it is a monolayer. When there are structural defects/phonon disorders in graphene, the D peak will arise at around 1350 cm^{-1}, which corresponds to the first order of different in-plane vibration modes. It should be noted that the first-order D peak is not visible in our graphene. The scanning electron microscopy (SEM) image of the graphene ring is shown in Fig. 1(a).

B. MAGNETOCONDUCTANCE MEASUREMENT

We measured the magnetoconductance oscillations in the fabricated graphene rings under out–of–plane magnetic fields up

to +/−2.1 T in an ultra-low-vibration cryogen-free closed-cycle cryostat at 4K. The magnetoconductance oscillations were measured in a two-terminal configuration, where the graphene structures were connected to the source-drain voltage supplies. The fabricated devices were wire-bonded onto a chip holder to measure the magnetoconductance in graphene rings inside the cryostat chamber. Magnetic sweeping was carried out while recording the conductance oscillations, which were processed to extract the AB oscillations from the magnetoconductance data. The fast-Fourier transform was used to determine the positions of the AB oscillation peaks of graphene rings, corresponding to the inner, average, and outer radius. The experimentally obtained peak positions were compared with simulation results.

III. RESULTS AND DISCUSSIONS

The schematic of a graphene ring is shown in Fig. 1(b), where the ring's inner radius is r_1, the average radius is $\bar{r}$, and the outer radius is r_2. The periodicity of the AB oscillations can be determined by

$$\Delta B = \frac{h}{e\pi r^2} \tag{1}$$

where r is the ring radius [35]. We compared the Fourier spectrum data obtained from the two-terminal magnetoconductance oscillations to the values calculated using (1). Here, we analyze the conductance data obtained from the graphene ring with an inner radius of 200 nm and arm width of 400 nm under the out-of-plane magnetic B-field ranging from −2 T to 2 T. The raw conductance data is shown in Fig. 2(a), from which one can see oscillations with a large amplitude and low frequency originating from the weak localization, the universal conductance fluctuations, the discrete Landau levels, and the edge effect [24].

The conductance oscillations due to AB interference should be several orders of magnitude smaller than these low-frequency oscillations at 4K. In order to extract the periodicity and the amplitude of the AB oscillations, we performed a baseline subtraction to denoise the measured signals. This baseline subtraction process has two steps: the baseline creation and the baseline subtraction. The baseline creation can be accomplished using Matlab with Wdenoise Toolbox. This toolbox denoises the data in X using the Block James-Stein method based on determining an optimal block size and threshold. The resulting block thresholding estimator yields simultaneously optimal global and local adaptivity [36]. The next step is the denoising procedure, which has three steps: 1) decomposition to choose both a wavelet and a level N, followed by the computation of the wavelet decomposition of the signal s at level N, 2) detail coefficient thresholding to select a threshold and apply soft thresholding to the detail coefficients for each level from 1 to N, and 3) reconstruction to compute wavelet reconstruction based on the original approximation coefficients of level N and the modified detail coefficients of levels from 1 to N. In this case, the smoothed curve generated is the noise in the study of the AB effect, since the magnitude

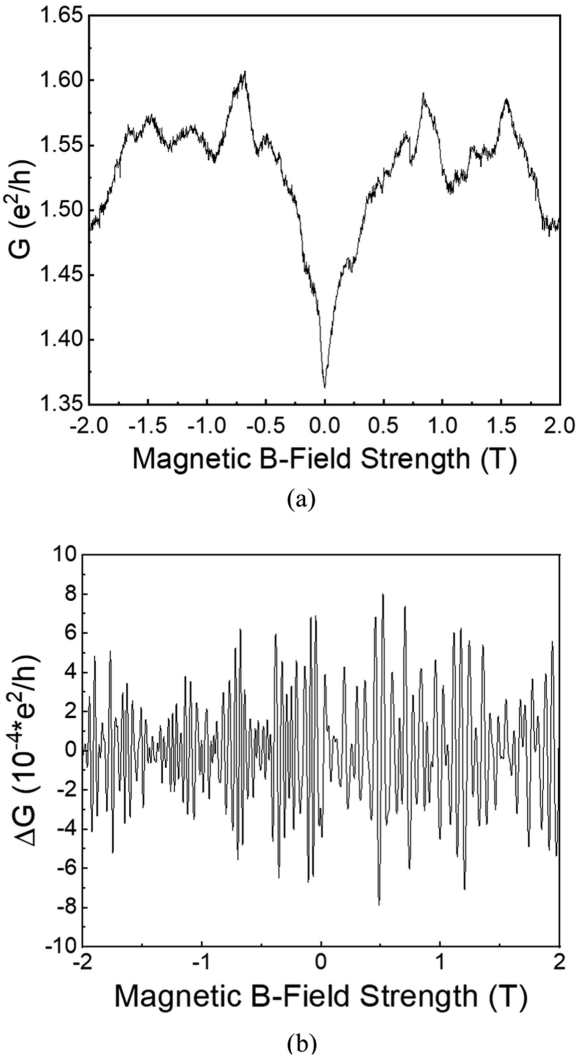

FIGURE 2. Magnetoconductance and AB oscillation of the graphene ring with a 200 nm inner radius and arm width of 400 nm measured at 4K (a) magnetoconductance of the graphene ring under the external out-of-plane magnetic B-field swept from −2 T to 2 T. (b) AB conductance oscillation extracted from (a) using the baseline subtraction method (curves are offset for clarity).

of the noise is much larger than the AB oscillation signals. The smoothed curve subtracts the raw data to obtain the AB oscillation signals. The extracted conductance oscillation of the ring with an inner radius of 200 nm and arm width of 400 nm is shown in Fig. 2(b).

The fast Fourier transform (FFT) was performed to analyze the AB oscillation signals from the processed data, as shown in Fig. 3. The FFT spectrum shows a relatively broad band that corresponds to the *h/e* mode signals of the ring, which are ranging from 30 to 273 1/T. The range of *h/e* and *h/2e* mode peaks are shown using dashed vertical lines. Based on (1), the peak periodicities of *h/e* mode corresponding to the inner radius (200 nm), average radius (∼400 nm), and outer radius (600 nm) are 30 1/T, 122 1/T, and 273 1/T, respectively. These values are labeled with green, blue, and black solid vertical lines. Next, we measured the conductance oscillations

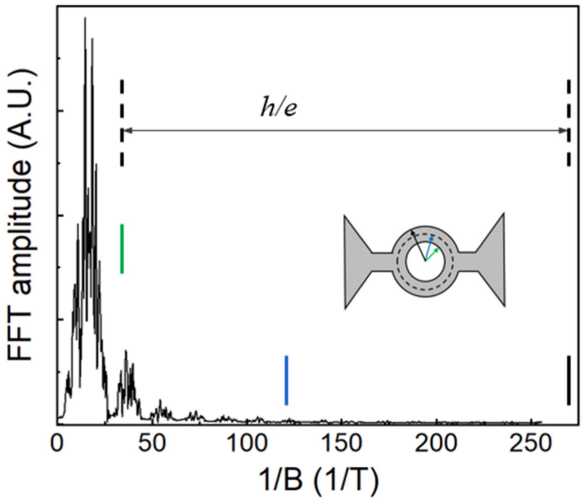

FIGURE 3. Fast Fourier transform spectrum of the AB oscillation obtained from the graphene ring with an inner radius of 200 nm and arm width of 400 nm. The vertical green and blue solid lines indicate the expected position of the h/e peaks, as determined from the inner and average radii of the ring, respectively. The inset schematic indicates a ring's inner, average and outer radii. The arrow labels the range of h/e peak. Due to the low scan speed (two data points per sec.) during the measurement, the h/e peak positions of the outer radius and most of the h/2e range are not shown.

of a ring with an inner radius of 400 nm and an arm-width of 400 nm under an out-of-plane magnetic field from 1.9 T to 2.1 T, in order to exclude the small B regime where large amplitude and low-frequency oscillations usually appear. Fig. 4(a) shows the conductance oscillations corresponding to the *h/e* mode through the inner radius (400 nm) of the graphene ring. Fig. 4(b) shows the Fourier spectrum of the experimental data, where the peak corresponding to the inner radius at 122 1/T is marked in a green vertical line. The blue and black vertical lines indicate the frequencies of the *h/e* mode peaks of the average and outer radii, 273 1/T and 488 1/T, respectively. We also label the range of *h/e* peaks with vertical dashed lines.

To further analyze the data, we employed the Kwant package [37] to systematically simulate the quantum magneto-transport dynamics of a monolayer graphene ring device. The tight-binding model with nearest-neighbor hopping was used to model the dynamics of the non-interacting electron system only, and the conductance was calculated as a function of the magnetic B-field strength. The conductance oscillations were significantly influenced by the Fermi energy choice, with the AB oscillations generally exhibiting more pronounced Fourier peaks in narrower rings with lower Fermi energies.

Fig. 5(a) presents a contour plot showcasing the magneto-conductance as a function of Fermi energy E and magnetic field B for a specific graphene ring geometry: inner radius $r_1 =$ 300 nm and outer radius $r_2 = 500$ nm. Additionally, the ring is attached to 200 nm wide left and right leads. To enhance the clarity of the AB oscillations, only the conductance simulation results for magnetic fields up to 0.6 T and E up to 1 meV are displayed, although the actual simulations extended up to 2 T and 29 meV. Our findings demonstrate the strong dependence

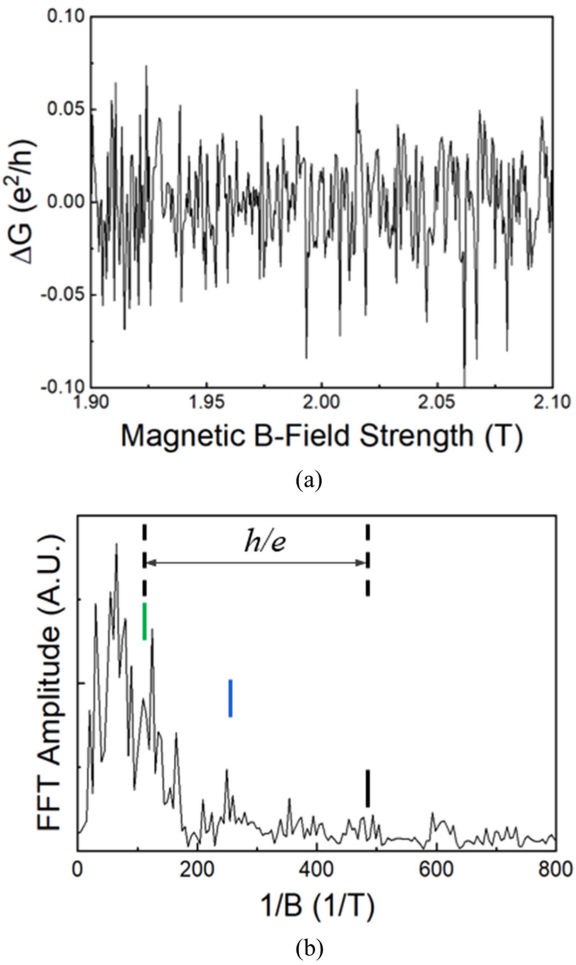

FIGURE 4. AB conductance oscillation and FFT spectra of the AB oscillations obtained from the graphene ring with an inner radius of 400 nm and arm width of 400 nm, measured at 4K under the external vertical magnetic B-field swept from 1.9 T to 2.1 T. (curves are offset for clarity). (a) AB conductance oscillation (b) Fourier spectrum. The solid green, blue, and black vertical lines indicate the positions of h/e peaks of the inner, average, and outer radii. The horizontal arrow indicates the range of h/e peak of the inner and outer radii.

of the conductance on the Fermi energy, which influences the number of conducting channels in the system. Note that the modeling did not consider structural defects, polymer residues, bulk disorder, edge states, spin-orbit coupling, top and side gate potentials, and temperature effects, which are expected to suppress the AB oscillations. Fig. 5(b) compares the Fourier spectra of the conductance for varying ring widths, ranging from 100 nm to 400 nm, with a fixed Fermi energy of 1 meV and a lead width of 100 nm. For the narrowest ring with 100 nm arm-width, we identify a pronounced peak corresponding to the magnetic flux quantum h/e determined by the average radius $r = 400$ nm. In Fig. 5(c), which is the enlarged view of the blue curve in Fig. 5(b), two side peaks appear, which are related to the interference between the two paths determined by the inner and outer radii of one arm and the average radius of the other arm. As the ring width increases, the main Fourier peaks shift to a higher frequency

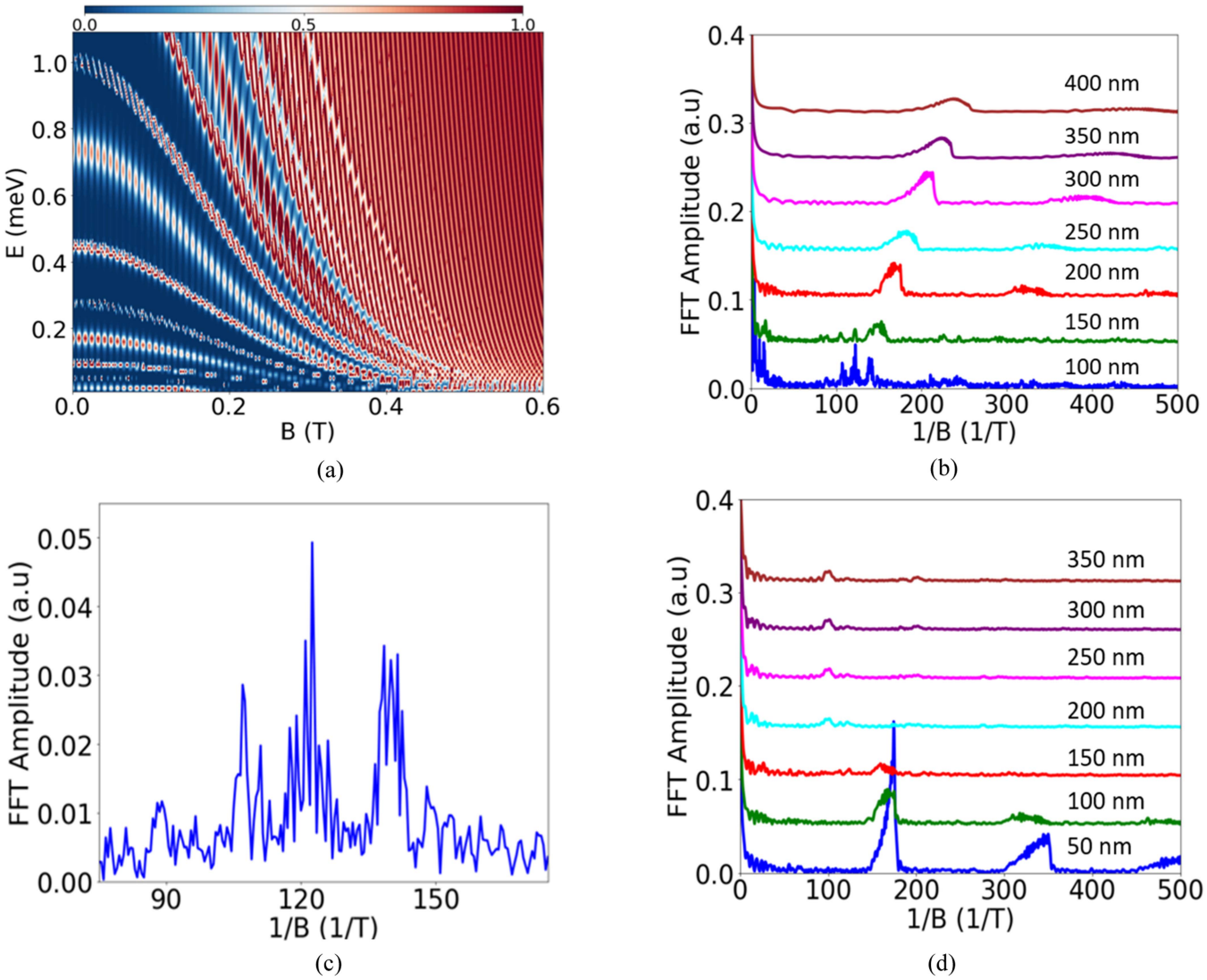

FIGURE 5. **Numerically computed conductance and FFT spectra of the AB oscillation. (a) Contour plot of the magnetoconductance as a function of the Fermi energy (E) and the magnetic field (B) for a graphene ring with average radius r = 400 nm, inner radius $r_1 = 300$ nm and outer radius $r_2 = 500$ nm, and attached to 200 nm wide left and right leads. (b) FFT spectra of the conductance for varying ring widths, ranging from 100 nm to 400 nm, (c) The zoom-in view of the FFT spectrum of the ring with 100 nm width. The fundamental mode exhibits three major peaks located at (i) 107/T, (ii) 122/T, and (iii) 138/T. These peaks arise due to the interference between two paths determined by (i) the inner radius of one arm and the average radius of the other arm, (ii) the average radius of the two arms, and (iii) the outer radius of one arm and average radius of the other arm, respectively, and (d) FFT spectra of the conductance for varying lead widths, ranging from 50 nm to 350 nm. Both spectra have a fixed Fermi energy of 1 meV and an average radius of 200 nm. The curves for different widths have been shifted for improved visualization.**

regime, exhibiting considerable broadening that smears out the individual oscillation side peaks. This correlation is anticipated as the quantum interference in wider rings involves electrons traversing closed paths enclosing a larger area than the average radius.

Moreover, with increased ring width, interferences can occur between numerous distinct paths, leading to a broadened spectrum. Fig. 5(d) compares the Fourier spectra of the conductance for varying lead widths, ranging from 50 nm to 350 nm, with a fixed Fermi energy of 1 meV and an average radius of 400 nm. A pronounced AB oscillation peak at around 160/T is identified when the width of the lead is smaller than the width of the ring. However, as the lead width surpasses this threshold, the peak diminishes, giving rise to a relatively minor AB oscillation peak at 100/T, which aligns with theoretical calculations based on the average radius. The numerical simulations presented in Fig. 5 demonstrate the intricate relationship between AB oscillations and the system geometry.

IV. CONCLUSION

We have demonstrated the fabrication and characterization of CVD-grown graphene rings. We demonstrated conductance measurements exhibiting phase-coherent electron transport in these graphene rings, with the observation of AB oscillations at 4K. We observed the fundamental mode (*h/e*) of

the AB conduction oscillations, corresponding to the average ring radius, as well as secondary modes related to the finite width of the graphene rings. These experimental observations were reproduced by numerical simulations that verified quasi-ballistic transport in our samples. This work shows AB oscillations in CVD-grown graphene rings at an elevated temperature (4K), compared to previous reports with exfoliated graphene rings.

REFERENCES

[1] T. Schumm et al., "Matter-wave interferometry in a double well on an atom chip," *Nature Phys.*, vol. 1, no. 1, pp. 57–62, 2005.

[2] B. Brezger, L. Hackermüller, S. Uttenthaler, J. Petschinka, M. Arndt, and A. Zeilinger, "Matter-wave interferometer for large molecules," *Phys. Rev. Lett.*, vol. 88, no. 10, 2002, Art. no. 100404.

[3] P. Haslinger, N. Dörre, P. Geyer, J. Rodewald, S. Nimmrichter, and M. Arndt, "A universal matter-wave interferometer with optical ionization gratings in the time domain," *Nature Phys.*, vol. 9, no. 3, pp. 144–148, 2013.

[4] Y. Bidel et al., "Absolute marine gravimetry with matter-wave interferometry," *Nature Commun.*, vol. 9, 2018, Art. no. 627.

[5] K. Fang, Z. Yu, and S. Fan, "Photonic Aharonov-Bohm effect based on dynamic modulation," *Phys. Rev. Lett.*, vol. 108, no. 15, 2012, Art. no. 153901.

[6] D. I. Chang et al., "Quantum mechanical complementarity probed in a closed-loop Aharonov–Bohm interferometer," *Nature Phys.*, vol. 4, no. 3, pp. 205–209, 2008.

[7] L. Vaidman, "Role of potentials in the Aharonov-Bohm effect," *Phys. Rev. A*, vol. 86, no. 4, 2012, Art. no. 40101.

[8] J. R. E. Toland and M. Zivkovic, "Sagnac effect in a chain of mesoscopic quantum rings," *Phys. Rev. A*, vol. 79, no. 5, 2009, Art. no. 053607.

[9] Y. Aharonov and D. Bohm, "Further considerations on electromagnetic potentials in the quantum theory," *Phys. Rev.*, vol. 123, no. 4, 1961, Art. no. 1511.

[10] M. Zivkovic, M. Jääskeläinen, and I. Djuric, "Sagnac rotational phase shifts in a mesoscopic electron interferometer with spin-orbit interactions," *Phys. Rev. B - Condens. Matter Mater. Phys.*, vol. 77, no. 11, 2008, Art. no. 115306.

[11] J. G. Rarity et al., "Two-photon interference in a Mach-Zehnder interferometer," *Phys. Rev. Lett.*, vol. 65, no. 11, 1990, Art. no. 1348.

[12] Y. Zhao, H. Zhao, R. Lv, and J. Zhao, "Review of optical fiber Mach–Zehnder interferometers with micro-cavity fabricated by femtosecond laser and sensing applications," *Opt. Lasers Eng.*, vol. 117, pp. 7–20, 2019.

[13] V. P. Ningrum et al., "Recent advances in two-dimensional magnets: Physics and devices towards spintronic applications," *Research*, vol. 2020, pp. 1–19, 2020.

[14] K. Shayan et al., "Magnetic proximity coupling of quantum emitters in WSe_2 to van der Waals ferromagnets," *Nano Lett.*, vol. 19, no. 10, pp. 7301–7308, 2019.

[15] X. Lin, W. Yang, K. L. Wang, and W. Zhao, "Two-dimensional spintronics for low-power electronics," *Nature Electron.*, vol. 2, no. 7, pp. 274–283, 2019.

[16] K. Liu et al., "Elastic properties of chemical-vapor-deposited monolayer MoS_2 , WS_2 , and their bilayer heterostructures," *Nano Lett.*, vol. 14, no. 9, pp. 5097–5103, 2014.

[17] A. Van Oudenaarden, M. H. Devoret, Y. V. Nazarov, and J. E. Mooij, "Magneto-electric Aharonov–Bohm effect in metal rings," *Nature*, vol. 391, no. 6669, pp. 768–770, 1998.

[18] S. Washburn, C. P. Umbach, R. B. Laibowitz, and R. A. Webb, "Temperature dependence of the normal-metal Aharonov-Bohm effect," *Phys. Rev. B*, vol. 32, no. 7, 1985, Art. no. 4789.

[19] T. Thakur and B. Szafran, "Aharonov-Bohm oscillations in phosphorene quantum rings: Mass anisotropy compensation by confinement potential," *Phys. Rev. B*, vol. 105, no. 16, 2022, Art. no. 165309.

[20] L. L. Li, D. Moldovan, P. Vasilopoulos, and F. M. Peeters, "Aharonov-Bohm oscillations in phosphorene quantum rings," *Phys. Rev. B*, vol. 95, no. 20, 2017, Art. no. 205426.

[21] B. Grbić, R. Leturcq, T. Ihn, K. Ensslin, D. Reuter, and A. D. Wieck, "Aharonov–Bohm oscillations in p-type GaAs quantum rings," *Physica E: Low-Dimensional Syst. Nanostructures*, vol. 40, no. 5, pp. 1273–1275, 2008.

[22] F. Miao, S. Wijeratne, Y. Zhang, U. C. Coskun, W. Bao, and C. N. Lau, "Phase-coherent transport in graphene quantum billiards," *Science*, vol. 317, no. 5844, pp. 1530–1533, 2007.

[23] M. Huefner et al., "Investigation of the Aharonov–Bohm effect in a gated graphene ring," *Physica Status Solidi (b)*, vol. 246, no. 11/12, pp. 2756–2759, 2009.

[24] D. Smirnov, H. Schmidt, and R. J. Haug, "Aharonov-Bohm effect in an electron-hole graphene ring system," *Appl. Phys. Lett.*, vol. 100, no. 20, 2012, Art. no. 203114.

[25] P. Recher, B. Trauzettel, A. Rycerz, Y. M. Blanter, C. W. J. Beenakker, and A. F. Morpurgo, "Aharonov-Bohm effect and broken valley degeneracy in graphene rings," *Phys. Rev. B*, vol. 76, no. 23, 2007, Art. no. 235404.

[26] J. Schelter, P. Recher, and B. Trauzettel, "The Aharonov–Bohm effect in graphene rings," *Solid State Commun.*, vol. 152, no. 15, pp. 1411–1419, 2012.

[27] J. Dauber et al., "Aharonov-Bohm oscillations and magnetic focusing in ballistic graphene rings," *Phys. Rev. B*, vol. 96, no. 20, 2017, Art. no. 205407.

[28] S. Russo et al., "Observation of Aharonov-Bohm conductance oscillations in a graphene ring," *Phys. Rev. B - Condens. Matter Mater. Phys.*, vol. 77, no. 8, 2008, Art. no. 085413.

[29] M. Huefner et al., "The Aharonov–Bohm effect in a side-gated graphene ring," *New J. Phys.*, vol. 12, no. 4, 2010, Art. no. 43054.

[30] J. Wurm, M. Wimmer, H. U. Baranger, and K. Richter, "Graphene rings in magnetic fields: Aharonov–Bohm effect and valley splitting," *Semicond. Sci. Technol.*, vol. 25, no. 3, 2010, Art. no. 34003.

[31] A. K. Geim and K. S. Novoselov, "The rise of graphene," *Nature Mater.*, vol. 6, no. 3, pp. 183–191, 2007.

[32] J.-Y. Moon et al., "Layer-engineered large-area exfoliation of graphene," *Sci. Adv.*, vol. 6, no. 44, 2020, Art. no. eabc6601.

[33] R. Saito, M. Hofmann, G. Dresselhaus, A. Jorio, and M. S. Dresselhaus, "Raman spectroscopy of graphene and carbon nanotubes," *Adv. Phys.*, vol. 60, no. 3, pp. 413–550, 2011.

[34] K. Kim et al., "Raman spectroscopy study of rotated double-layer graphene: Misorientation-angle dependence of electronic structure," *Phys. Rev. Lett.*, vol. 108, no. 24, 2012, Art. no. 246103.

[35] D. J. Griffiths, "Introduction to electrodynamics," *Amer. J. Phys.*, vol. 73, no. 6, p. 574, 2005.

[36] T. T. Cai, "On block thresholding in wavelet regression: Adaptivity, block size, and threshold level," *Statistica Sinica*, vol. 12, pp. 1241–1273, 2002.

[37] C. W. Groth, M. Wimmer, A. R. Akhmerov, and X. Waintal, "Kwant: A software package for quantum transport," *New J. Phys.*, vol. 16, no. 6, 2014, Art. no. 63065.

ZITAO TANG received the B.S. degree in chemistry from the University of California at Berkeley, Berkeley, CA, UAS, and the M.S. degree in mechanical engineering in 2020 from the Stevens Institute of Technology, Hoboken, NJ, USA, where he is currently working toward the Ph.D. degree in mechanical engineering. His research focuses on the fabrication of the FET structures based on graphene and the applications of 2D materials.

SIWEI CHEN, photograph and biography not available at the time of publication.

CYNTHIA I. OSUALA received the M.S. degree in theoretical and applied physics from the African University of Science and Technology, Galadima, Nigeria, in 2019. She is currently working toward the Ph.D. degree in physics with the Stevens Institute of Technology, Hoboken, NJ, USA. Her research interests include quantum transport in electronics, photonics, and topological insulators.

ABDUS SALAM SARKAR, photograph and biography not available at the time of publication.

GRZEGORZ HADER, photograph and biography not available at the time of publication.

ARON CUMMINGS, photograph and biography not available at the time of publication.

STEFAN STRAUF, photograph and biography not available at the time of publication.

CHUNLEI QU, photograph and biography not available at the time of publication.

EUI-HYEOK YANG (Senior Member, IEEE) received the Ph.D. degree in microelectromechanical systems (MEMS) from Ajou University, South Korea, in 1996, and the Master of Engineering degree (*honoris causa)* from the Stevens Institute of Technology, Hoboken, NJ, USA, in 2023. He was a postdoctoral scholar first with the University of Tokyo, Tokyo, Japan, and then with the Caltech. In 1999, he joined NASA's Jet Propulsion Laboratory (JPL), and became a Senior Member of the engineering staff in 2001. He joined the Department of Mechanical Engineering, Stevens Institute of Technology, as an Associate Professor in 2006, and became a Professor in 2014. His group's research focuses on growth and nanofabrication of 2D ferromagnetic materials for spintronics. At JPL, he led several projects funded by NASA, DARPA, and NRO, and managed and monitored several NASA SBIR projects and participated in the review committee for developing NASA's Multi-Object Spectrometer for the James Webb Space Telescope. He secured over forty federal grants and contracts totaling approximately $11M, including the NSF, AFOSR, NRO, and US Army funding. He has authored or coauthored more than three hundred fifty journal and conference papers and has been invited to give over a hundred keynote/invited talks at conferences, workshops, and university seminars. He is an associate editor or editorial board member of *Scientific Reports*, *Micromachines*, and IEEE SENSORS JOURNAL. He was a featured Track Plenary Speaker at ASME IMECE in 2018. Among other honors, he was awarded the Lew Allen Award for Excellence at JPL in 2003, the Award for Research Excellence at Stevens in 2019, and the IEEE Technical Achievement Award (Advanced Career) from the IEEE Sensors Council in 2020. He is an IEEE Sensors Council Distinguished Lecturer during 2023–2025, and IEEE Nanotechnology Council (NTC) Chapter Chair (North Jersey Section). Dr. Yang is a Fellow of the National Academy of Inventors. He is also a Fellow of the American Society of Mechanical Engineers.